

OpenGGCM Simulations for the THEMIS Mission

Joachim Raeder · Douglas Larson · Wenhui Li ·
Emil L. Kepko · Timothy Fuller-Rowell

Received: 17 March 2008 / Accepted: 18 July 2008
© Springer Science+Business Media B.V. 2008

Abstract The THEMIS mission provides unprecedented multi-point observations of the magnetosphere in conjunction with an equally unprecedented dense network of ground measurements. However, coverage of the magnetosphere is still sparse. In order to tie together the THEMIS observations and to understand the data better, we will use the Open Geospace General Circulation Model (OpenGGCM), a global model of the magnetosphere-ionosphere system. OpenGGCM solves the magnetohydrodynamic (MHD) equations in the outer magnetosphere and couples via field aligned current (FAC), electric potential, and electron precipitation to a ionosphere potential solver and the Coupled Thermosphere Ionosphere Model (CTIM). The OpenGGCM thus provides a global comprehensive view of the magnetosphere-ionosphere system. An OpenGGCM simulation of one of the first substorms observed by THEMIS on 23 March 2007 shows that the OpenGGCM reproduces the observed substorm signatures very well, thus laying the groundwork for future use of the OpenGGCM to aid in understanding THEMIS data and ultimately contributing to a comprehensive model of the substorm process.

Keywords THEMIS · OpenGGCM · Magnetosphere · MHD · Simulation · Substorm

J. Raeder (✉) · D. Larson · W. Li · E.L. Kepko
Space Science Center, University of New Hampshire, Durham, NH, USA
e-mail: J.Raeder@unh.edu

D. Larson
e-mail: Douglas.Larson@unh.edu

W. Li
e-mail: wenhuil@cisunix.unh.edu

E.L. Kepko
e-mail: Larry.Kepko@unh.edu

J. Raeder
Physics Department, University of New Hampshire, Durham, NH, USA

T. Fuller-Rowell
CIRES, Colorado University, Boulder, CO, USA
e-mail: Tim.Fuller-Rowell@noaa.gov

1 Introduction

The substorm debate has been a central part of space physics for over four decades and centers on the question of what physical process(es) precipitate the sudden energy release in the magnetotail and the sudden auroral brightening and expansion (Akasofu 1977; Lui 1991; Fairfield 1992; Kennel 1992; McPherron 1991; Baker et al. 1999).

It is probably fair to say that it is widely accepted that substorms are ultimately powered by magnetic reconnection. Reconnection signatures are often observed in the tail during the course of substorms. However, the location of the associated x -lines is typically observed $\sim 20R_E$ from Earth or further down the tail. Conversely, the initial brightening of the aurora maps much closer to Earth. Thus, the question is commonly posed as to whether reconnection causes the process that brightens the aurora or whether the process that brightens the aurora causes reconnection. The THEMIS mission (Sibeck and Angelopoulos 2008; Angelopoulos 2008) is designed to answer this question by providing simultaneous measurements at five locations in order to establish how events proceed in time and space.

However, in spite of the unprecedented coverage, ambiguities will likely remain because processes such as dipolarization of the field or earthward flows may not necessarily occur strictly radially but sweep azimuthally over the spacecraft, creating an apparent radial motion that does not correspond to the real one. Furthermore, substorms come in different sizes and shapes, and at this point it is only a hypothesis that they all follow the same scheme. It is well known that some substorms are triggered by various solar wind or IMF changes while others occur spontaneously. Furthermore, there are other forms of geomagnetic activity such as pseudo-breakups and Steady Magnetospheric Convection (SMC) events, that have some traits of substorms but differ in certain aspects. THEMIS will undoubtedly clarify the phenomena and the relationships between different forms of activity and substorm triggers. However, the physical processes will not be understood fully until we are able to model them.

We will thus complement the THEMIS mission with global simulations of the magnetosphere. While it is possible to use local models to study isolated processes such as reconnection in detail, it is not possible to apply local models to substorms. Substorms are inherently global and encompass physical processes ranging from the dayside magnetopause, the lobes, the plasma sheet, and the inner magnetosphere to the ionosphere and to the ground. There have been a few attempts in the past to model substorms with global models, such as the “GEM substorm challenge” (Slinker et al. 1995; Fedder et al. 1995; Wiltberger et al. 2000; Raeder and Maynard 2001; Raeder et al. 2001b). None of these simulations has been able to reproduce a substorm in its entirety. Some substorm-related phenomena such as particle injections are beyond the MHD description of the models. However, even the phenomena that global MHD based models should be able reproduce do often not come out well. For example, all models have a tendency to enter an SMC-like state, where nightside reconnection closely balances dayside reconnection and no loading-unloading cycle occurs. Models then often require tweaking of parameters for a substorm to occur (Raeder et al. 2001b). The necessity for such tweaking reflects the multi-scale nature of substorms, i.e., the effects of small-scale processes, such as anomalous resistivity, kinetic instabilities, or other processes that break the frozen flux condition. Such processes are not included self-consistently in the model, but they are represented, at least to some extent, by parameterizations. As long as self-consistent treatment of such small-scale processes in global models is not possible, one hopes that these parameterizations are good enough to capture the substorm physics correctly. In essence, these parameterizations constitute hypotheses concerning the underlying physical processes, and, by comparison of the model

results with in situ data, we test them. We present one example of such a comparison later in this paper which shows a quite reasonable agreement with the data. However, many more such studies are needed to firmly establish the validity of the model.

We will thus use the OpenGGCM in at least three different ways to support THEMIS and to better understand substorms:

1. We will test and constrain the model by simulating a number of substorm events with THEMIS (and other) observations. These simulations will be driven with observed solar wind and IMF data which are usually available from solar wind monitors such as ACE or Wind. The output of these simulations will be critically compared, timetrace by timetrace, to the observations to find out what the model captures well and what it does not. Of course, the comparisons will never be perfect, and in many cases not good at all. We will run different simulations for one event with varying parameters, such as numerical resolution, M-I coupling parameters (see below), different anomalous resistivity, and different sub-models (ionosphere, ring current.) From these runs we expect learn what parameters are important and how to choose them to get the physics right. We will also learn where we can trust the model, and which outputs will most likely differ from reality. In Sect. 3 below we present an example, the 23 March 2007 substorm, which shows that the OpenGGCM correctly predicts several aspects of this substorm, but not all.
2. Based on verification of the results as outlined above we will use the OpenGGCM results to help interpret the THEMIS data. THEMIS observations are still spotty and leave large gaps in the spatial coverage, which can be filled with model results. The OpenGGCM can also provide relationships that are generally not observable, such as the mapping between the plasma sheet and the ionosphere. This mapping has also been done in the 23 March 2007 substorm example shown below. It turns out that magnetic mapping using the OpenGGCM explains the observations much better than mapping based on empirical models (Angelopoulos et al. 2008).
3. The magnetosphere cannot be controlled and manipulated like a laboratory experiment; it can only be observed passively. Simulations, on the other hand, can be controlled within certain limits. For example, it is possible to use different solar wind and IMF, but it is not possible to reduce diffusion or resistivity below the inherent numerical diffusivities. We will thus use the OpenGGCM for numerical experiments to test hypotheses; for example, how solar wind and IMF changes trigger substorms, and how the ionosphere controls convection and the substorm process.

In the end, we hope that a new and more coherent picture of the substorm process will emerge from the THEMIS data in conjunction with OpenGGCM simulations. Without the simulations, the THEMIS data will likely leave ambiguities, while without the data the simulations would be essentially speculation.

In the remaining sections we first describe the OpenGGCM in detail. Then we present first results of the 23 March 2007 substorm event, which is also discussed in a companion paper (Angelopoulos et al. 2008). That section also serves to illustrate some of the outputs that the OpenGGCM can produce. The last section summarizes our results and provides an outlook.

2 The OpenGGCM Model

The OpenGGCM is a global coupled model of Earth's magnetosphere, ionosphere, and thermosphere. The magnetosphere part solves the MHD equations as an initial-boundary-value problem. The MHD equations are only solved to within $\sim 3R_E$ of Earth. The region

within $3R_E$ is treated as a magnetosphere-ionosphere (MI) coupling region where physical processes that couple the magnetosphere to the ionosphere-thermosphere system are parameterized using simple models and relationships. The ionosphere – thermosphere system is modeled using the NOAA CTIM (Coupled Thermosphere Ionosphere Model, Fuller-Rowell et al. 1996; Raeder et al. 2001a). In the following we describe each part of the model in more detail.

2.1 Outer Magnetosphere

The physics of the outer magnetosphere is governed by the magnetohydrodynamic equations, which we use in their normalized, semi-conservative form:

$$\frac{\partial \rho}{\partial t} = -\nabla \cdot (\rho \mathbf{v}) \quad (1)$$

$$\frac{\partial \rho \mathbf{v}}{\partial t} = -\nabla \cdot (\rho \mathbf{v} \mathbf{v} + p \mathbf{l}) + \mathbf{j} \times \mathbf{B} \quad (2)$$

$$\frac{\partial e}{\partial t} = -\nabla \cdot (\{e + p\} \mathbf{v}) + \mathbf{j} \cdot \mathbf{E} \quad (3)$$

$$\frac{\partial \mathbf{B}}{\partial t} = -\nabla \times \mathbf{E} \quad (4)$$

$$\nabla \cdot \mathbf{B} = 0 \quad (5)$$

$$\mathbf{E} = -\mathbf{v} \times \mathbf{B} + \eta \mathbf{j} \quad (6)$$

$$\mathbf{j} = \nabla \times \mathbf{B} \quad (7)$$

$$e = \frac{\rho v^2}{2} + \frac{p}{\gamma - 1} \quad (8)$$

The symbols have their usual meaning, e.g., \mathbf{B} and \mathbf{E} are the magnetic and the electric field, respectively, \mathbf{v} is the plasma velocity, ρ is the density, p is the pressure, \mathbf{j} is the current density, η is a resistivity, \mathbf{l} is the unit tensor, and γ is the ratio of specific heats.

The semi-conservative formulation is chosen because it allows for finite difference schemes that numerically conserve mass (ρ), momentum ($\rho \mathbf{v}$), and plasma energy (e), but with no strict conservation of total energy. Fully conservative schemes that conserve total energy ($U = \frac{p}{\gamma - 1} + \frac{\rho v^2}{2} + \frac{B^2}{2}$) often suffer from instability in low β regions where the pressure must be computed as the difference of two large quantities (U and $B^2/2$). The semi-conservative form avoids this difficulty.

The solution of the MHD equations in the outer magnetosphere is accomplished using an explicit second-order predictor-corrector finite difference time stepping scheme. The spatial derivatives are also computed using finite differences. However, because the simulation involves super-magnetosonic flows and shocks, simple finite differences are not sufficient but flux-limited schemes must be used. In the case of the OpenGGCM, we use a hybrid scheme that was originally proposed by Harten (Harten and Zwas 1972), where we combine a fourth-order scheme with a minimal diffusion error (Zalesak 1979, 1981) with the diffusive first-order Rusanov scheme. The numerical switch ensures that we obtain a high-order solution in regions of smooth variation of the flow, i.e., where there are no discontinuities, which degrades to a low-order solution at discontinuities, such as shocks and contacts, where the high-order scheme would fail due to numerical dispersion. Such shock-capturing schemes

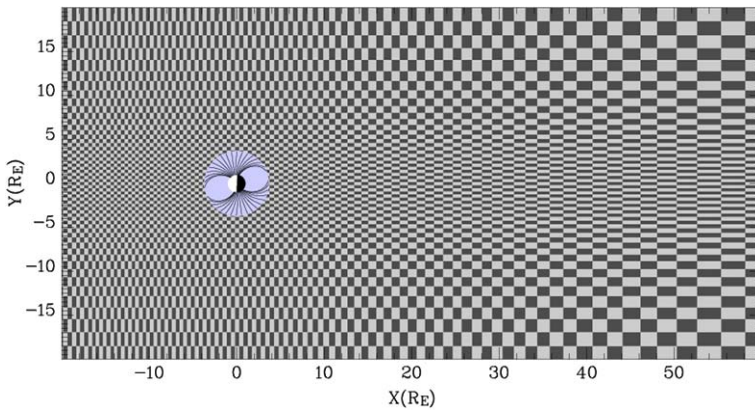


Fig. 1 Section of the OpenGGCM numerical grid. The grid is Cartesian but non-uniform in each of the coordinate directions. This figure shows only a fraction of the grid, which normally extends several hundred R_E anti-sunward, and $\sim 40R_E$ in each of the y - and z -directions. Also, the resolution is generally much finer (by a factor 2–3 in each direction) than shown here

are common in computational fluid dynamics of trans-sonic and supersonic flows (Hirsch 1990; Laney 1998).

Maxwell's equation states that $\nabla \cdot \mathbf{B} = 0$ at all times, since there are no magnetic monopoles. Strictly speaking, this is only an initial condition for \mathbf{B} because Faraday's law demands that if $\nabla \cdot \mathbf{B} = 0$ at some time, it is to remain so as the magnetic field evolves, which can be seen from:

$$\nabla \cdot \frac{\partial \mathbf{B}}{\partial t} = \frac{\partial(\nabla \cdot \mathbf{B})}{\partial t} = -\nabla \cdot \nabla \times \mathbf{E} = 0 \quad (9)$$

Many numerical schemes do not a priori preserve $\nabla \cdot \mathbf{B}$. For such schemes the accumulation of $\nabla \cdot \mathbf{B}$ can lead to serious errors, in particular spurious parallel acceleration, wrong magnetic topology (field lines that are not closed), and significant errors in the shock jumps (Brackbill and Barnes 1980; Toth 2000). There are a few methods to clean the magnetic field of monopoles, for example the projection method, but none of these is perfect, and they also incur substantial additional cost (Toth 2000). The OpenGGCM uses the Constrained Transport (CT) method introduced by Evans and Hawley (Evans and Hawley 1988), which employs a staggered grid that allows near perfect (to roundoff error) preservation of $\nabla \cdot \mathbf{B}$. With CT, the magnetic field components are put on cell faces, and the electric field components for the right hand side of Faraday's law are put on the centers of the cells' edges. Such staggered grids require interpolation for the coupling terms $\mathbf{j} \times \mathbf{B}$ and $\mathbf{j} \cdot \mathbf{E}$; however, this is a small price to pay for magnetic flux conservation.

An important aspect of every MHD code is the spatial grid. Many choices are possible, ranging from equidistant Cartesian grids to structured adaptive mesh refinement (AMR) grids (see Raeder 2003, for an overview and discussion of grids). The OpenGGCM employs a stretched Cartesian grid. Figure 1 shows a cut through the grid in the x - y plane at $z = 0$. The figure shows only part of the grid; typically the grid extends to $\sim 20R_E$ in the sunward direction (to the left), several $100R_E$ in the anti-sunward direction (to the right), and $\sim 40R_E$ in the transverse (y and z) directions. Also, the grid resolution is substantially better than Fig. 1 indicates, typically 0.1 – $0.2R_E$ at the sub-solar magnetopause and 0.2 – $0.3R_E$ in the near-Earth tail, with a total of 10^7 – 10^8 grid cells.

The primary advantage of the OpenGGCM grid is that it allows for a well load balanced and efficient parallelized code, while it, for the most part, optimizes the resolution where it is needed. A uniform Cartesian grid would need 10^2 – 10^3 times the number of cells to achieve the same resolution in critical regions, such as the magnetopause or the plasma sheet. On the other hand, non-Cartesian or AMR grids may be able to optimize resolution better, but they also incur a higher computational cost and require much more complex codes.

2.2 Ionosphere and MI Coupling

As outlined above, the MHD calculation only extends to $\sim 3R_E$ from Earth. At that inner boundary the MHD part of the model is coupled with the ionosphere, mainly by the closure of field-aligned currents (FACs) in the ionosphere. The OpenGGCM uses a static dipole model to map the FACs into the ionosphere, which is possible for two reasons: (1) the current density obeys a continuity equation and (2) these currents typically do not close across field lines at this altitude. At the ionosphere end, a potential equation is solved on a sphere (or a section thereof) to yield the ionospheric convection potential (Fedder and Lyon 1987). The potential is then mapped back to the inner boundary of the MHD calculation where it is used as boundary condition for the flow and field integration ($\mathbf{v} = (-\nabla\Phi) \times \mathbf{B} / |\mathbf{B}|^2$). Because the mapping originates at $3R_E$, it covers the latitudes from $\sim 58^\circ$ to 90° .

The dipole orientation is kept fixed in the OpenGGCM; i.e., the dipole does not rotate. Its orientation is set to the real geophysical dipole orientation at a given time, which is usually chosen to match a specific event. For studies of short-lived phenomena such as a substorm, there is no significant drawback in keeping the dipole orientation fixed, since the dipole does not rotate much during the period of interest. However, the fixed dipole orientation is less realistic for long duration events such as magnetic storms. During such events the largest error would occur at times that are an odd number of half-days different from the time that the dipole orientation corresponds to, and the error could be as large as twice the offset of the magnetic pole from the geographic pole, i.e., $\sim 22^\circ$. This error affects mainly the dayside reconnection geometry because it alters the shear angle between the IMF and the dipole field.

The ionosphere-thermosphere model CTIM is described in detail elsewhere (see Fuller-Rowell et al. 1996, and references therein); thus we only provide a brief description here. CTIM is a global multi-fluid model of the thermosphere-ionosphere system with a long heritage. CTIM solves both neutral and ion fluid equations self-consistently from 80 to 500 km for the neutral atmosphere and from 80 to 10,000 km for the ionosphere on a spherical grid with 2° latitude resolution and 18° longitude resolution. The thermosphere part solves the continuity equation, horizontal momentum equation, energy equation, and composition equations for the major species O, O₂, and N₂ on 15 pressure levels. The ionosphere model part solves the continuity equations, ion temperature equation, vertical diffusion equations, and horizontal transport for H⁺ and O⁺, while chemical equilibrium is assumed for N₂⁺, O₂⁺, NO⁺, and N⁺. The horizontal ion motion is governed by the magnetospheric electric field. The coupled model includes about 30 different chemical and photo-chemical reactions between the species. Compared to the magnetosphere, the CTIM time scales are relatively long, allowing for numerical time steps of the order of one minute. Consequently, CTIM is computationally very efficient and runs considerably faster than real-time (> 10 times) on a single CPU.

CTIM's primary input are the solar UV and EUV flux (parameterized by the solar 10.7 cm radio flux), the tidal modes (forcing from below), auroral electron precipitation parameters, and the magnetospheric electric field.

The electron precipitation parameters, energy flux F_E , and mean energy E_0 are computed separately for diffuse precipitation and for discrete precipitation, i.e., for electrons accelerated in regions of upward FAC.

Diffuse precipitation is parameterized by:

$$F_E = n_e(kT_e/2\pi m_e)^{\frac{1}{2}}, \quad E_0 = kT_e \tag{10}$$

where T_e and n_e are the magnetospheric electron temperature and density, respectively, and k is the Boltzmann constant.

Discrete electron precipitation is modeled using the Knight relation (Knight 1972):

$$\Delta\Phi = K \max(0, -j_{\parallel}) \tag{11}$$

$$K = \frac{e^2 n_e}{\sqrt{2\pi m_e k T_e}} \tag{12}$$

$$F_E = \Delta\Phi_{\parallel} j_{\parallel}, \quad E_0 = e\Delta\Phi_{\parallel} \tag{13}$$

where $\Delta\Phi$ is the parallel potential drop on an auroral field line. Because the MHD model cannot provide an electron temperature, we use the MHD single fluid temperature adjusted by a fudge factor.

The electric field in the ionosphere is assumed to be a potential field and is obtained from current conservation, which leads to the following potential equation (Vasyliunas 1970; Kelley 1989):

$$\nabla \cdot \Sigma \cdot \nabla\Phi = -j_{\parallel} \sin I \tag{14}$$

with the boundary condition $\Phi = 0$ at the magnetic equator. Because the ionosphere is a magnetized and partially ionized plasma, the ionospheric conductance is a tensor (Strange-way and Raeder 2001), given by:

$$\Sigma = \begin{pmatrix} \Sigma_{\theta\theta} & \Sigma_{\theta\lambda} \\ -\Sigma_{\theta\lambda} & \Sigma_{\lambda\lambda} \end{pmatrix} \tag{15}$$

$$\Sigma_{\theta\theta} = \frac{\Sigma_P}{\sin^2 I}, \quad \Sigma_{\theta\lambda} = \frac{\Sigma_H}{\sin I}, \quad \Sigma_{\lambda\lambda} = \Sigma_P \tag{16}$$

where Σ_H is the Hall conductance, Σ_P is the Pedersen conductance, θ is the magnetic latitude, λ is the magnetic longitude, and I is the magnetic field inclination.

The ionospheric Hall and Pedersen conductance is computed by CTIM from first principles, i.e., from the electron-neutral collision terms. In addition, the neutral wind dynamo is explicitly included in the solution of the electric potential. The neutral dynamo plays no significant role during substorms, but can produce a flywheel effect during storms, where the neutrals are accelerated by ion drag during the storm main phase, while the neutrals impart momentum on the ions during the recovery phase and thereby generate an electric field (Rishbeth et al. 1991). Using the CTIM conductances, as opposed to using conductances from empirical models, significantly affects the simulations. The effect of different conductance models in the OpenGGCM and its predecessors has been studied previously (Raeder et al. 1996, 2001a). The latter study showed that the model produced significantly more realistic ionosphere potentials in runs where the MHD model was coupled with CTIM. Although that study focused on storms, we have also conducted simulation runs with different

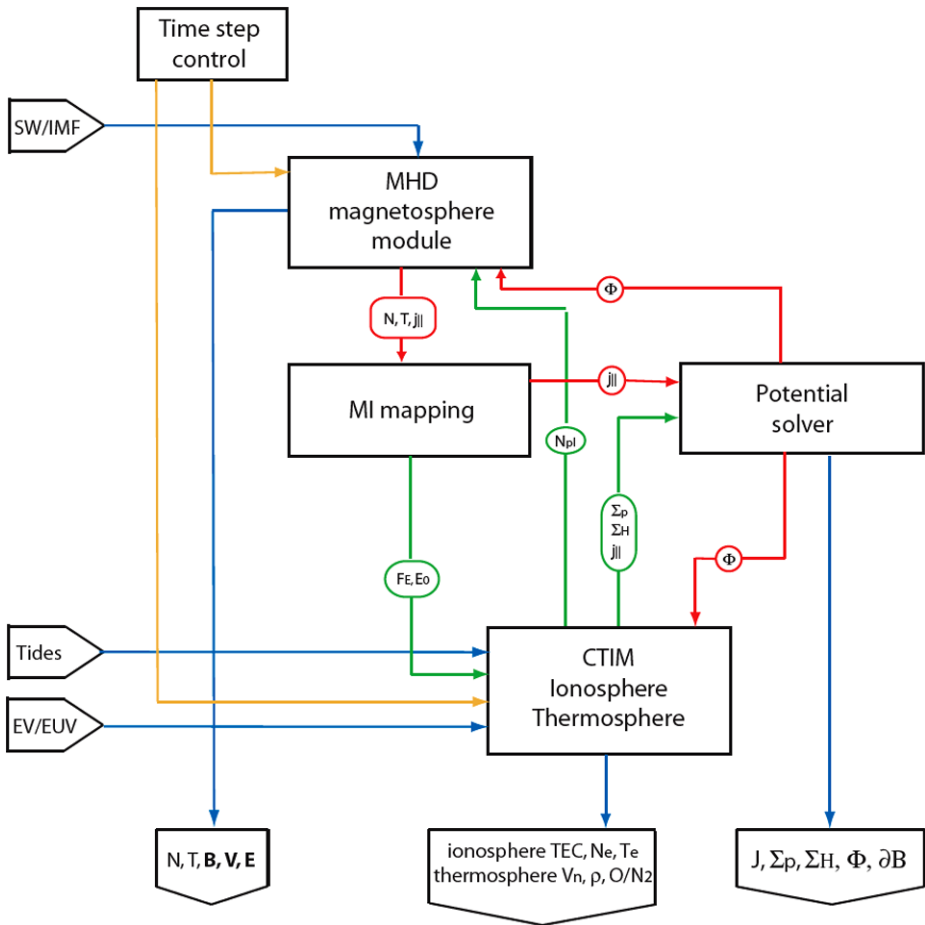


Fig. 2 Block diagram of the OpenGGCM with its models and with data/control flow. *Blue lines* denote model input and output. *Red lines* denote data flow with strong coupling. *Green lines* denote data flow with weak or slow coupling. *Orange lines* denote control flow. B , N , and T are the magnetospheric magnetic field, plasma density, and temperature, respectively. The field aligned current is $j_{||}$, Φ is the ionosphere potential, F_E and E_0 the energy flux and mean energy of precipitating electrons, Σ_H and Σ_P the ionosphere Hall and Pedersen conductances, and ∂B is the ground magnetic perturbation

conductance models for the 23 March 2007 substorm presented later in this paper. Here we also find that the simulation results from the coupled model are in much better agreement when the CTIM conductances are used. Conversely, when uniform conductance is used, or when the nightside e^- precipitation is switched off in CTIM, only a weak substorm or no substorm at all may develop in the simulation.

Figure 2 shows a block diagram of the OpenGGCM elements and their relationships. The connection arrows indicate the flow of data. Note that the OpenGGCM only requires a minimal set of inputs. The solar wind and IMF are typically taken from a solar wind monitor such as ACE or Wind. Geotail and Cluster can also provide SW and IMF data when they are upstream of the bow shock. Such data taken closer to Earth are preferable because they better represent the solar plasma and fields that ultimately interact with the magnetosphere. However, even these data are not perfect as input for the OpenGGCM because they generally lack

information about the three-dimensional solar wind structure, which must be known ideally, to specify the time-dependent MHD variables across the entire inflow boundary. We thus need to make an assumption as to the structure of the solar wind. One option is to assume that the solar wind parameters are independent of Y_{GSE} and Z_{GSE} . In that case, the IMF B_x component cannot change in time because that would violate $\nabla \cdot \mathbf{B} = 0$. If there are significant IMF B_x variations, the assumption of Y_{GSE} and Z_{GSE} independence cannot be true. In that case, we attempt to find a direction \mathbf{N} in the solar wind such that the magnetic field component along that direction (B_N) does not change significantly. Since usually only one solar wind monitor is available, we employ the minimum variance method of Sonnerup and Cahill (1967, 1968) to find that direction. We call this the MINVAR method. If observations from multiple solar wind monitors are available, more precise methods are available (see, for example Russell et al. 2001). If B_N is fairly constant over the time interval of interest, we set B_N to be constant in time at the value of its average and then transform the field back into GSE coordinates and use it as input to the MHD model. In this case the solar wind and IMF convects into the model as sheets whose orientation is given by their normal vector \mathbf{N} .

In the case that B_N from the minimum variance transform is not nearly uniform (defined such that the variance of B_N is significantly smaller, say $< 10\%$ of the total field) the solar wind does not have a simple sheet-like structure and there is also not enough information available to determine the structure. The options are to either ignore the IMF B_x component or to set it to some constant value that seems reasonable. This may in many cases not be a bad choice, because the IMF B_x component essentially does not contribute to the interplanetary electric field (IEF) and because the draping of the IMF around the magnetosphere normally reduces the B_x component before the field interacts with the magnetosphere. However, if the IMF B_x component dominates the IMF it may affect the reconnection geometry at the magnetopause and the simulation results must be carefully assessed for their validity.

Figure 3 shows the time series of the solar wind and IMF data observed by Wind for the 23 March 2007 substorm along with the data that have been processed using the MINVAR procedure. The top panel shows the B_L (maximum variance, red line), B_M (intermediate variance, green line), and B_N (minimum variance, blue line) IMF components. The eigenvector (direction) corresponding to the minimum variance \mathbf{N} is given at the top of the figure. The direction of \mathbf{N} is close to sunward but has a significant Z component. For this case the variance of the B_N component is small compared to the total field; thus the IMF must at least be ordered locally in sheets that are normal to \mathbf{N} . There are several discontinuities, i.e., rapid changes in the IMF direction, in this interval. Since B_N across these discontinuities is close to zero, they are most likely tangential discontinuities.

The following three panels show the three IMF components. The red lines show the Wind observations. The blue lines show the result from setting B_N to zero and transforming back to GSE. The green lines show the result from setting B_N to its average over the entire interval and transforming back to GSE. For each component the three lines nearly coincide. The near coincidence of the green and blue lines simply reflects the fact that the B_N average is nearly zero for this interval. The near coincidence of the red and green traces shows that the IMF model of inclined planar sheets whose normal is \mathbf{N} is consistent with the data.

The bottom two panels of Fig. 3 show the solar wind plasma parameters. These time series are not affected by the MINVAR procedure. However, in order to be consistent with the treatment of the plasma parameters they are convected into the simulation box in the same manner as the field components; i.e., the MHD state vector $\mathbf{U} = (\mathbf{B}, \mathbf{V}, N, T)$ at the inflow boundary is not just a function of time $\mathbf{U}(t)$, but also a function of Y_{GSE} and Z_{GSE} ($\mathbf{U}(y, z, t)$) to take the inclined sheet structure of the solar wind and IMF into account.

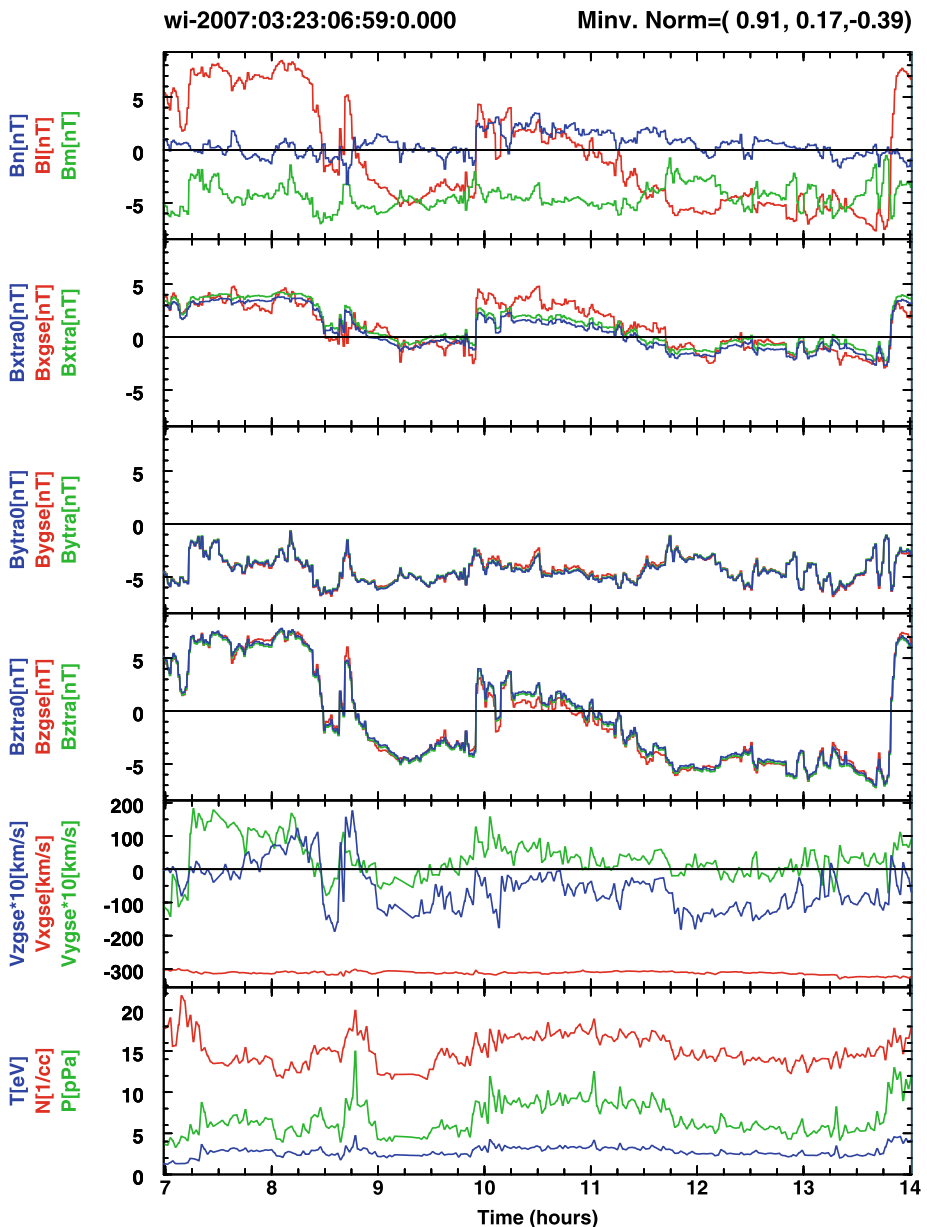


Fig. 3 Solar wind and IMF data processed by the MINVAR procedure and used as input for the simulation of the 23 March 2007 substorm event

3 OpenGGCM Products and the 23 March 2007 Substorm Example

The OpenGGCM produces the three-dimensional grids with the MHD state vector (ρ , p , \mathbf{V} , \mathbf{B}), along with a number of ionosphere and thermosphere quantities, such as the ionosphere potential, ionospheric currents, electron density, neutral composition,

and neutral winds. These quantities describe the state of the system; however, they often cannot be directly compared to observations, and the information contained in the gridded fields is too overwhelming to see the physical processes that occur and to draw conclusions. The output of a simulation run can easily exceed one TB (terabyte, equal to 10^{12} bytes) of data. Thus, in order to extract useful information, a substantial amount of post-processing and visualization is necessary. There are many ways to extract information from the raw data, and new techniques are still being developed. In the following we demonstrate some of the most basic techniques and applications. We will use an OpenGGCM simulation of the 23 March 2007 substorm as an example. This substorm is also discussed elsewhere in this issue (Angelopoulos et al. 2008; Keiling et al. 2008), and thus we will not discuss the observations here but direct the reader to these papers.

3.1 Satellite Time Series

The most basic comparison is that of the moments and fields measured at the satellite with the time series taken in the simulation at the same location. We refer to these time series as “virtual satellites.” In version 3.1 of the OpenGGCM, these time series are automatically generated for a number of satellites (made up or real) and their trajectories, which are input to the model. This approach has the advantage that the time series output can be generated at high cadence (~ 5 s) but it does not allow re-positioning the virtual satellite after the run is completed. The latter approach, i.e., generating time series from three-dimensional output at a location that is somewhat displaced from the true satellite location, is sometimes useful when a satellite is located close to a boundary. In that case a small error in the boundary location can lead to a complete mismatch between the observations and the virtual satellite. By placing a second virtual satellite at the other side of the boundary, often just by a fraction of $1R_E$, one can then show that the boundary location is primarily in error, not the MHD state variables themselves.

Figures 4, 5, and 6 show the comparison of the virtual satellites THEMIS C, THEMIS B, and THEMIS E with the in situ observations. THEMIS C is the closest to the tail center, THEMIS E is the closest to the dusk flank, and THEMIS D, B, and A are located very close together between C and E, and thus observe nearly the same, at least on the MHD time scale. The companion paper (Angelopoulos et al. 2008) discusses the locations in detail.

All three satellites observe a flow burst, both tailward and duskward, near the time of the substorm onsets, which was determined by Angelopoulos et al. (2008) to occur at 10:54 UT (minor activation) and 11:19 UT (major activation). At the same time the magnetic field becomes strongly deflected. That deflection is similar but not the same as a classical dipolarization. The B_z and B_y components increase as in a dipolarization; however, the magnitude of B_x also increases, which is opposite to dipolarization. Furthermore, the sunward flows sweep colder and denser plasma past the spacecraft.

The virtual spacecraft see essentially the same signatures, but with some significant differences. First, the substorm onset, as defined by the onset of fast flows here, occurs too early ($\sim 10:40$ UT) as opposed to the 10:54 UT and 11:19 UT onsets and intensifications observed by THEMIS and the imagers (see Angelopoulos et al. 2008, this issue). This is also borne out in the aurora from the simulation discussed further below. However, the general pattern of the magnetic field and flow variations are quite well reproduced. Plasma density and temperature match least well, which can be understood as a memory effect of the magnetosphere. This simulation was started at 07:00 UT, i.e., four hours before the substorm onset, thus

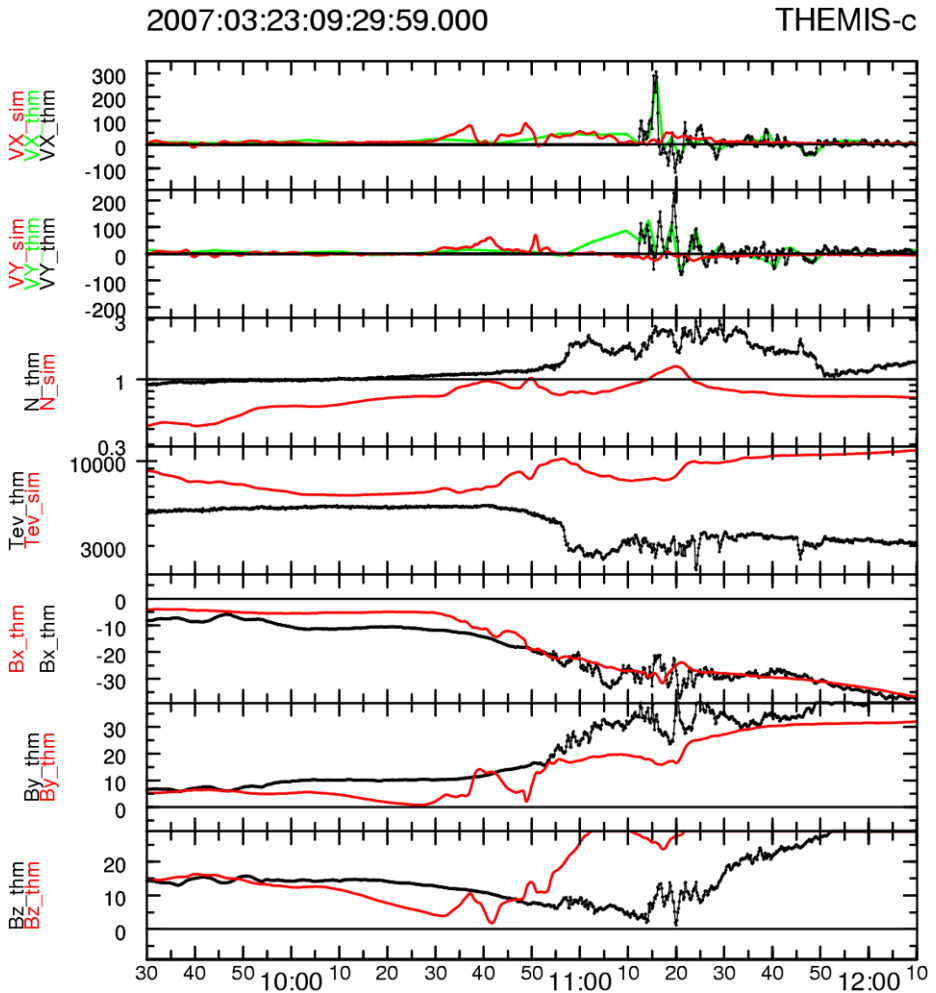


Fig. 4 Comparison of the MHD state variables measured by THEMIS C (*black and green lines*, the latter from on-board computation of moments) and from the OpenGGCM simulation (*red lines*). The panels show, from *top to bottom*: the three components of the velocity, the plasma number density, the ion temperature, and the three components of the magnetic field. All variables are in GSE coordinates. THEMIS C is the closest to the tail center

much of the plasma in the simulated magnetosphere may still be primordial, i.e., a remnant from the initial conditions. How long it takes for the magnetosphere to completely replenish all of its plasma from the solar wind and ionospheric sources is not well known and probably depends on the solar wind and IMF conditions.

Overall the simulation reproduces the key observational features well enough for there to be confidence in the results. In particular, a reasonable comparison like this one can be the starting point for a more detailed analysis of the simulation in order to elucidate the processes that lead to the observed phenomena.

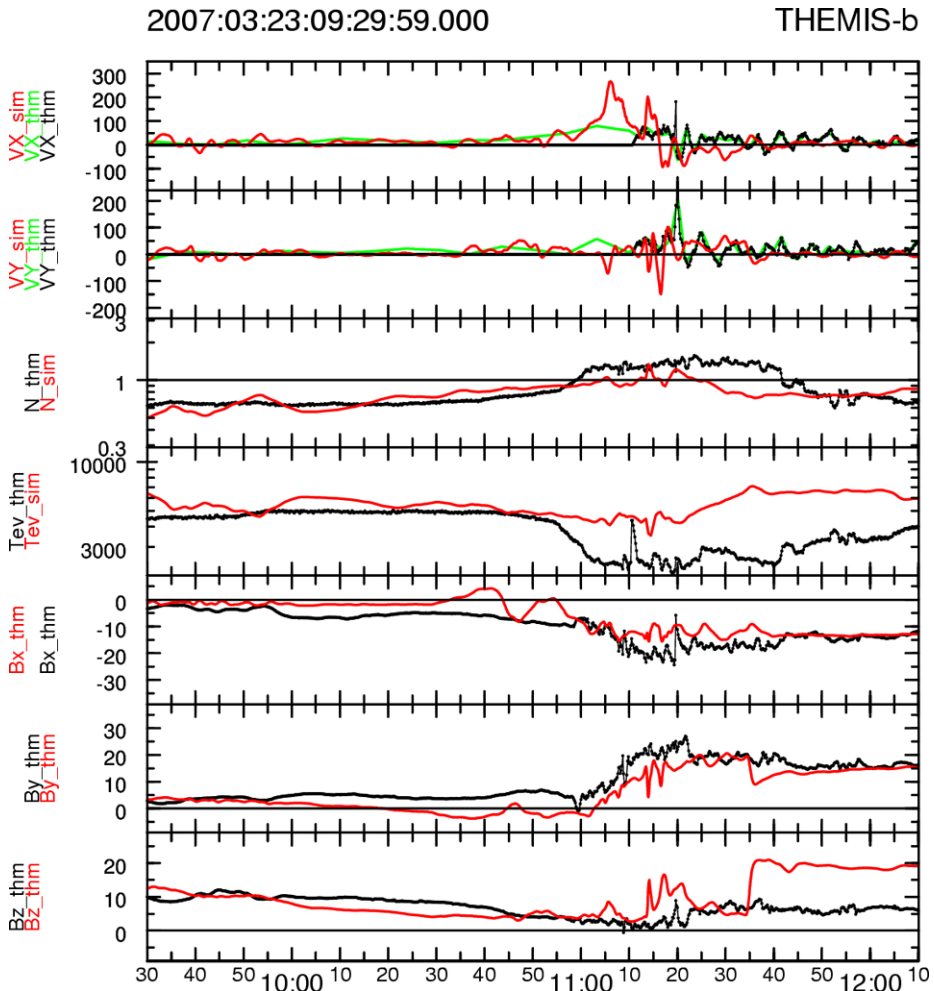


Fig. 5 Comparison of the MHD state variables measured by THEMIS B in the same format as Fig. 4. THEMIS B is the middle spacecraft between C and E

3.2 Ionosphere and Aurora

Of course, the defining characteristic of a substorm is the brightening of the aurora and the development of the westward traveling surge (WTS) (Akasofu 1964, 1977). The OpenGGCM does not produce auroral emissions; however, it does produce the energy flux and the mean energy of two populations of precipitating electrons. The first population is the thermal electron flux from the inner magnetosphere, which is unstructured and representative of the diffuse aurora. The second population is made up of electrons that have been accelerated in regions of upward flowing field-aligned current (FAC), as discussed in Sect. 2. This population is highly structured and it is considered generating the discrete aurora, although that distinction may not be made from an experimental view. In high resolution OpenGGCM runs such as the one presented here, features in the discrete precipitation as small as $\sim 0.5^\circ$ in latitude and $\sim 2^\circ$ in longitude can be resolved. In the plots discussed below

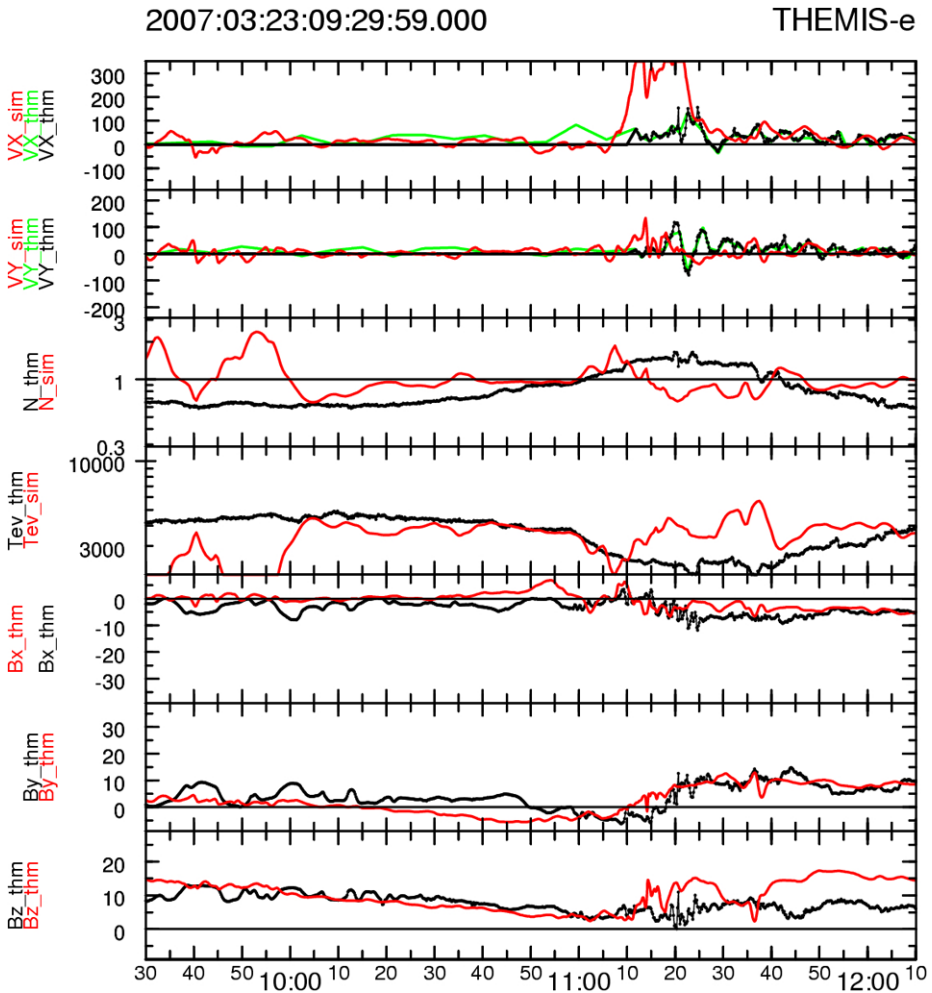


Fig. 6 Comparison of the MHD state variables measured by THEMIS E in the same format as Fig. 4. THEMIS E is the spacecraft the closest to the dusk flank

we show the energy flux of these accelerated electrons as a proxy for auroral emissions. In principal the emissions could be calculated (Emery et al. 1996; Germany et al. 1997; Lummerzheim et al. 1997). However, in order to be able to compare the emissions to data the specific instrument responses need to be modeled, which has not been done here.

Figure 7 shows a polar view of the northern hemisphere at six different times. Each of the six panels shows the energy flux of precipitating electrons color coded in units of mW/m^2 . The thick black line shows the polar cap boundary, i.e., the boundary between open and closed magnetic flux. Each panel has the date and the UT time indicated in the upper left corner.

At 10:00 UT the IMF at the magnetopause is still northward, and thus the magnetosphere is in a geomagnetically quiet state. The polar cap (PC) is small, with the PC boundary (PCB) mostly located between 75° and 80° magnetic latitude. At 10:40 UT the IMF has turned southward at the dayside magnetopause. The PC has expanded considerably, with

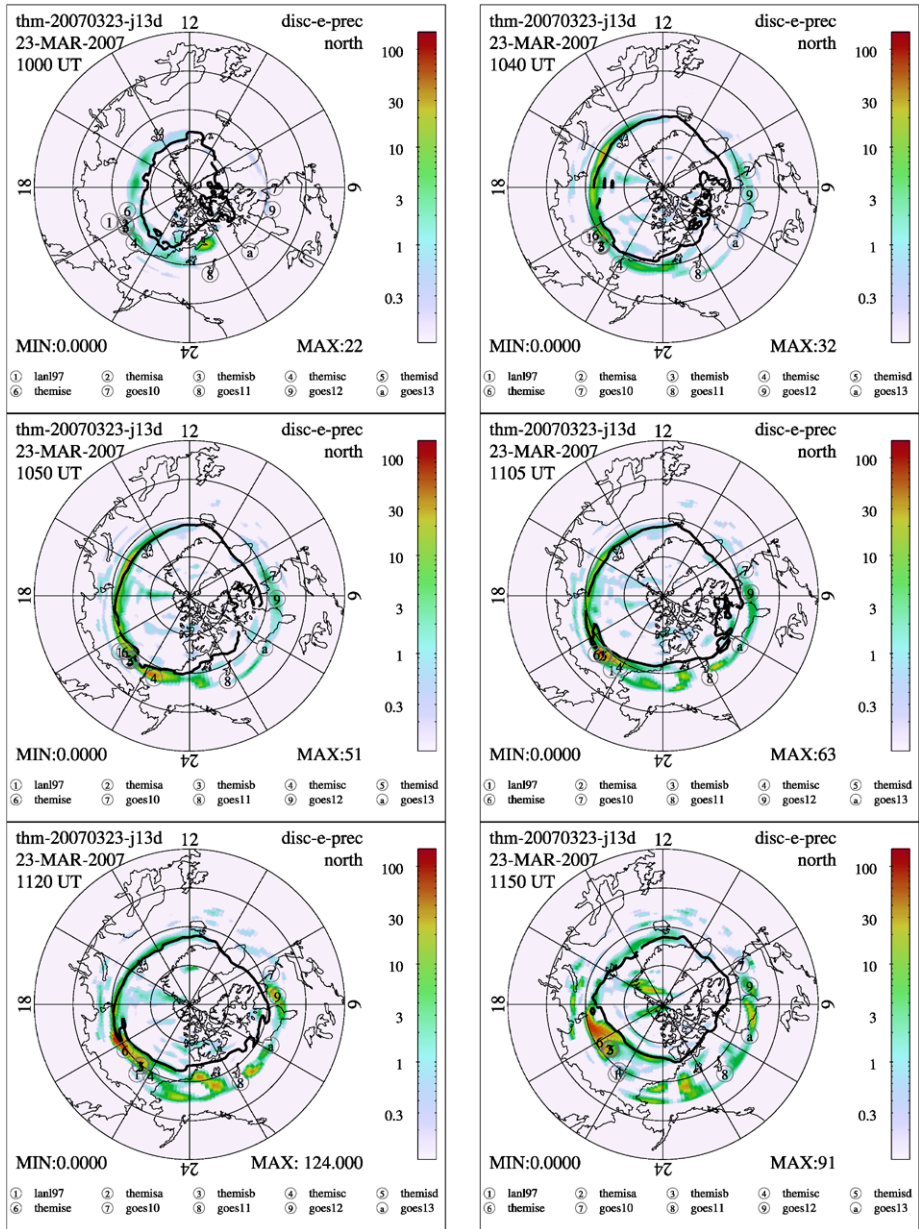


Fig. 7 Polar view of the northern hemisphere. The color coding shows the energy flux of accelerated electrons, which serves as a proxy for auroral emissions. The *thick black line* is the polar cap boundary

the PCB located just above 70° at most local times. This state represents the growth phase of the substorm, i.e., magnetic energy is being convected into and stored in the tail lobes. As the tail lobes expand, so does the PC, and at the same time the magnetic flux and magnetic energy in the lobes ($B^2/2\mu_0$) increases. During the quiet time and during the growth phase, the discrete aurora occurs primarily just equatorward of the PCB.

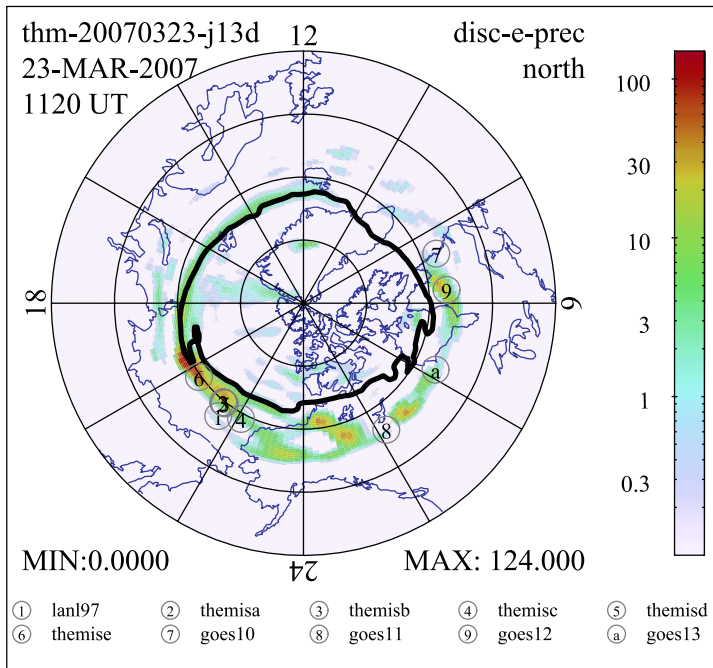


Fig. 8 Panel 5 of Fig. 7 at a larger size. The magnetic footpoints of several satellites show that the THEMIS probes map right into the westward traveling surge

At 10:50 UT the first indication of a substorm onset becomes visible near 22.5 MLT and 68° magnetic latitude. Closer inspection of the time series of polar plots shows that this intensification already started at 10:44 UT. This is considerably earlier than the first onset in the data, where the first intensification occurred at $\sim 10:54$ UT, followed by intensifications at $\sim 11:10$ UT and $\sim 11:19$ UT (Angelopoulos et al. 2008). The next panel shows that by 11:05 UT the aurora had expanded northward by $\sim 3^\circ$ and westward to ~ 21 MLT. Close inspection of the following 10 min (not shown here) shows that the expansion slows down and stops. However, between 11:15 UT and 11:20 UT, another intensification starts that causes a significant further expansion westward to ~ 19 MLT and $\sim 77^\circ$ magnetic latitude, as can be seen in the 5th and 6th panels. This latter expansion appears to correspond to the 11:19 UT expansion observed in the data. Comparison with the IMF data shown in Fig. 3 indicates that this intensification is likely caused by the sharp northward turn of the IMF at 09:55 UT. The Wind data need to be time shifted by ~ 75 min to account for the convection time from the Wind location ($X_{GSE} = 198R_E$) to the magnetopause, which means that the arrival of the northward turning at the magnetopause occurs at $\sim 11:10$ UT. There is considerable uncertainty in the actual arrival time because Wind is off the sun—Earth line by $\sim 30R_E$.

In Fig. 7 the magnetic mapping from the THEMIS (and several other) satellites to the ionosphere is marked. The 5th panel of Fig. 7 is shown as Fig. 8 for clarity. The THEMIS probes map magnetically into the path of the WTS. This result is expected because of the flow and field signatures observed by THEMIS and on the ground. However, magnetic mapping using an empirical magnetic field model places the THEMIS probes east and south

of the WTS (Angelopoulos et al. 2008), and thus the OpenGGCM mapping is much more realistic.

3.3 Magnetosphere Flow and Field Evolution

In order to understand the physical processes that trigger the expansion phase onset and provide the power in the expansion phase, at least as they happen in the model, an analysis of the complete three-dimensional data sets from the simulation is needed. The huge data sets in 4 dimensions, i.e., 3 space dimensions and time, make this a difficult task. The simulation of the substorm shown here has $\sim 30 \times 10^6$ cells, and at least a few hundred snapshots in time are needed to obtain a complete picture. Furthermore, there are at least the eight MHD state variables per cell, and in practice a number of derived variables, such as current density or electric field require examination. In all, the simulation leads to 10^{11} to 10^{13} data values, which are impossible to comprehend altogether. Furthermore, contemporary data presentation techniques and tools are mostly restricted to a two-dimensional “flatland” (paper or computer screen) which requires a substantial reduction and projection of the data (Tufté 1990). Occasionally the time dimension can be added with movies or animations, but even in there only some 3-dimensional hyperspaces can be seen out of the 4-dimensional data that matter.

Figure 9 shows three three-dimensional renderings of the magnetosphere in the vicinity of the THEMIS probes. Each rendering is composed of three cut planes (at $X_{GSE} = 0R_E$, $Y_{GSE} = 0R_E$, $Z_{GSE} = -2R_E$), which are color coded according to a physical quantity, such as B_z in the $Z_{GSE} = -2R_E$ plane and $\log(T)$ in the other two planes. The $Z_{GSE} = -2R_E$ also shows arrows that depict the flow velocity. These arrows are scaled to \sqrt{V} in order to cover a large dynamic range of speeds. The sphere centered on the origin has a radius of $3.5R_E$ and coincides with the inner boundary of the MHD simulation. Its surface is also color coded, in this case with the Hall conductance, which has been mapped along dipole field lines from the ionosphere. A number of field lines are drawn as pink tubes. One set of field lines originates from 65° magnetic latitude, at every 7.5° longitude. These field lines are all dipolar and mostly undisturbed. They provide a good idea of the dipole orientation. A second set of field lines is seeded along the X -axis in the tail. These field lines are obviously highly dynamic. Satellites of interest are pictured by spheres, and field lines are drawn through them. In Fig. 9, these satellites are, in order of decreasing distance, THEMIS E, A, B, D, C, and LANL97, which is a geosynchronous satellite and the closest to the Earth. Finally, there is a pink iso-surface that depicts sunward flows in excess of 180 km/s.

The top panel of Fig. 9 shows the magnetosphere at 10:30 UT, which is during the substorm growth phase. At this time the B_z in the plasma sheet is positive; i.e., the plasma sheet is on closed field lines. However, the field is not simply dipolar but is significantly stretched. Also, the negative IMF B_y exerts a twist on the tail which is clearly visible. The flows in the plasma sheet are mostly calm and of the order of a few 10s km/s.

The second panel shows the tail during the first substorm activation at 10:45 UT. There is now a significant patch of negative B_z in the plasma sheet at $X_{GSE} \sim -20R_E$ and somewhat duskward of the tail center. This negative B_z is also accompanied by strong tailward flows of several 100 km/s. Note that a negative B_z closer to Earth can also arise from the dipole tilt and the fact that the $Z_{GSE} = -2R_E$ plane does not coincide everywhere with the center of the plasma sheet. Such negative B_z comes from southern lobe field lines that bend toward the Earth into the southern polar cap. Coincident with the tailward flows are also earthward flows closer to Earth. These are not visible in the $Z_{GSE} = -2R_E$ plane, but in the iso-surface that extends earthward of the reconnection site. At this time not much has happened at the

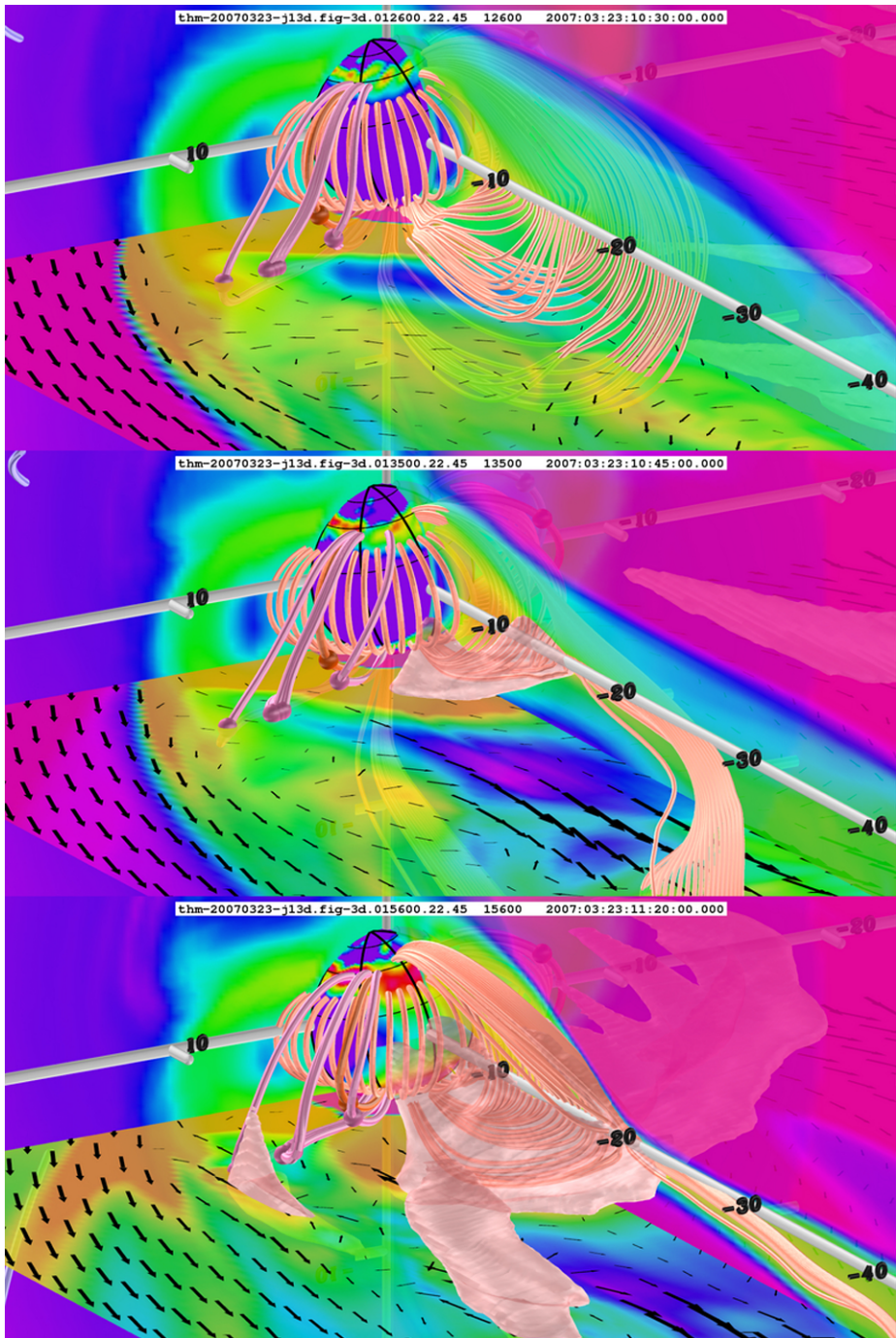


Fig. 9 Three-dimensional rendering of the magnetosphere configuration in the vicinity of the THEMIS probes during the 23 March 2007 substorm event. See text for a detailed explanation

THEMIS and LANL locations, but there are clear enhancements visible in the ionosphere Hall conductance. These occur because a substorm current wedge has formed that causes enhanced electron precipitation in the ionosphere at ~ 22 MLT.

The bottom panel shows the tail at 11:20 UT, just after the second intensification. At this time, the field near midnight has already dipolarized. There is now a new reconnection event further duskward. This event also creates a patch of strong southward IMF and both earthward/sunward and tailward flows. Most importantly, the sunward flows engulf the THEMIS spacecraft and cause the field at the spacecraft to dipolarize. Comparison with Figs. 4–6 shows that these flows and the dipolarization of the field are indeed observed.

Although Fig. 9 reveals a lot about the structure of the tail and its time evolution, it only shows some very limited aspects of the physical processes occurring in the simulation and will still require a substantial amount of work in the future. Replacing the sequence of the snapshots in time with a movie can give a much better impression of the dynamics of the plasma sheet. However, even then, the careful selection of the visualizing elements, such as cut planes or field lines is crucial to show the dynamical evolution.

4 Summary and Conclusions

In this paper we presented a description of the OpenGGCM and its role in supporting the THEMIS mission. For the simulations to be useful we first need to show that the model indeed produces the observed dynamical changes in the magnetosphere and ionosphere. The comparison of the model results with observations will never be perfect. However, as long as the model produces the essential features, the resulting confidence in the model allows conclusions to be drawn from the model results. We have presented here the first of such comparisons and shown that the model reproduces most of the salient features of the 23 March 2007 substorm. We have shown how the model can contribute to the mission and data analysis, in this case by providing the magnetic mapping between the ionosphere and the plasma sheet. We also provided a first glimpse at how the model results might be used to investigate the physical processes that ultimately lead to the observations.

In the future many more comparisons between the model and data need to be done to firmly establish what the model gets right and what it does not. With that background, the OpenGGCM can then be used to analyze the underlying physics, at least at the macro-scale, in more detail. Furthermore, the model can be used to conduct numerical experiments and to ask specific questions. For example, we may use the model to establish what mechanism leads to substorm triggering by northward turnings of the IMF. Comparing a run with a substorm triggered by a NBZ turn to one that is otherwise identical but without NBZ turn should provide the clues. Similarly, we may investigate the role that various parameters play in the onset mechanism, such as anomalous resistivity or ionosphere conductance. Such studies should eventually lead to a clearer and less controversial picture of the substorm process.

Acknowledgements This research was supported by NASA grant NAS5-02099. Development of the OpenGGCM has been supported by NASA grant NNG05GM57G and NSF grants ATM-0639658. Part of the simulations were performed at the San Diego Supercomputer Center and at the National Center for Supercomputer Applications.

References

S.-I. Akasofu, The development of the auroral substorm. *Planet. Space Sci.* **12**, 273 (1964)

- S.-I. Akasofu, *Physics of Magnetospheric Substorms* (Reidel, Dordrecht, 1977)
- V. Angelopoulos, The THEMIS mission. *Space Sci. Rev.* (2008, this issue). doi:[10.1007/s11214-008-9336-1](https://doi.org/10.1007/s11214-008-9336-1)
- V. Angelopoulos et al., First results from the THEMIS mission. *Space Sci. Rev.* (2008, this issue). doi:[10.1007/s11214-008-9378-4](https://doi.org/10.1007/s11214-008-9378-4)
- D.N. Baker, T.I. Pulkkinen, J. Büchner, A.J. Klimas, Substorms: A global instability of the magnetosphere-ionosphere system. *J. Geophys. Res.* **104**, 14,601 (1999)
- J.U. Brackbill, D.C. Barnes, The effect of nonzero div B on the numerical solution of the magnetohydrodynamic equations. *J. Comput. Phys.* **35**, 426 (1980)
- B.A. Emery et al., Comparing POLAR UVI imager data and other conductance sources in AMIE. *Eos Trans. AGU* **77**(46), 613 (1996)
- C.R. Evans, J.F. Hawley, Simulation of magnetohydrodynamic flows: A constrained transport method. *Astrophys. J.* **332**, 659 (1988)
- D.H. Fairfield, Advances in magnetospheric storm and substorm research: 1989–1991. *J. Geophys. Res.* **97**, 10,865 (1992)
- J.A. Fedder, J.G. Lyon, The solar wind-magnetosphere-ionosphere current-voltage relationship. *Geophys. Res. Lett.* **14**, 880 (1987)
- J.A. Fedder, S.P. Slinker, J.G. Lyon, R.D. Elphinstone, Global numerical simulation of the growth phase and the expansion onset for a substorm observed by Viking. *J. Geophys. Res.* **100**, 19,083 (1995)
- T.J. Fuller-Rowell, D. Rees, S. Quegan, R.J. Moffett, M.V. Codrescu, G.H. Millward, A coupled thermosphere-ionosphere model (CTIM), in *STEP Report*, ed. by R.W. Schunk (Scientific Committee on Solar Terrestrial Physics (SCOSTEP), NOAA/NGDC, Boulder, 1996), p. 217
- G.A. Germany, G.K. Parks, M. Brittnacher, J. Cumnock, D. Lummerzheim, J.F. Spann, L. Chen, P.G. Richards, F.J. Rich, Remote determination of auroral energy characteristics during substorm activity. *Geophys. Res. Lett.* **24**, 995 (1997)
- A. Harten, G. Zwas, Self-adjusting hybrid schemes for shock computations. *J. Comput. Phys.* **9**, 568 (1972)
- C. Hirsch, *Numerical Computation of Internal and External Flow*, vol. II (Wiley, New York, 1990)
- A. Keiling et al., Correlation of substorm injections, auroral modulations, and ground Pi2. *Geophys. Res. Lett.* **35**, L17S22 (2008). doi:[10.1029/2008GL033969](https://doi.org/10.1029/2008GL033969)
- M.C. Kelley, *The Earth's Ionosphere* (Academic Press, New York, 1989)
- C.F. Kennel, The Kiruna conjecture: The strong version, in *Substorms I*, vol. SP-335 (ESA, Noordwijk, 1992), p. 599
- S. Knight, Parallel electric fields. *Planet. Space Sci.* **21**, 741 (1972)
- C.B. Laney, *Computational Gasdynamics* (Cambridge University Press, Cambridge, 1998)
- A.T.Y. Lui, Extended consideration of a synthesis model for magnetic substorms, in *Magnetospheric Substorms*, ed. by J.R. Kan, T.A. Potemra, S. Kokubun, T. Ijima. *AGU Geophys. Monogr. Ser.*, vol. 64 (American Geophysical Union, Washington, 1991), p. 43
- D. Lummerzheim, M. Brittnacher, D. Evans, G.A. Germany, G.K. Parks, M.H. Rees, J.F. Spann, High time resolution study of the hemispheric power carried by energetic electrons into the ionosphere during the May 19/20, 1996 auroral activity. *Geophys. Res. Lett.* **24**, 987 (1997)
- R.L. McPherron, Physical processes producing magnetospheric substorms and magnetic storms, in *Geomagnetism*, vol. 4, ed. by J. Jacobs (Academic Press, New York, 1991), p. 593
- J. Raeder, Global magnetohydrodynamics—A tutorial, in *Space Plasma Simulation*, ed. by J. Büchner, C.T. Dum, M. Scholer (Springer, Berlin, 2003)
- J. Raeder, N. Maynard, Foreword. *J. Geophys. Res.* **106**, 345 (2001)
- J. Raeder, J. Berchem, M. Ashour-Abdalla, The importance of small scale processes in global MHD simulations: Some numerical experiments, in *The Physics of Space Plasmas*, vol. 14, ed. by T. Chang, J.R. Jasperse (MIT Cent. for Theoret. Geo/Cosmo Plasma Phys., Cambridge, 1996), p. 403
- J. Raeder, Y.L. Wang, T. Fuller-Rowell, Geomagnetic storm simulation with a coupled magnetosphere—ionosphere—thermosphere model, in *Space Weather*, ed. by P. Song, G. Siscoe, H.J. Singer. *AGU Geophys. Monogr. Ser.*, vol. 125 (American Geophysical Union, Washington, 2001a), p. 377
- J. Raeder et al., Global simulation of the geospace environment modeling substorm challenge event. *J. Geophys. Res.* **106**, 381 (2001b)
- H. Rishbeth, W. Deng, R.G. Roble, T.L. Killeen, A.G. Burns, The flywheel effect: ionospheric currents after a geomagnetic storm. *Geophys. Res. Lett.* **18**, 1845 (1991)
- C.T. Russell, Y.L. Wang, J. Raeder, The interplanetary shock of September 24, 1998: Arrival at Earth. *J. Geophys. Res.* **105**, 25,143 (2001)
- D.G. Sibeck, V. Angelopoulos, THEMIS science objectives and mission phases. *Space Sci. Rev.* (2008, this issue). doi:[10.1007/s11214-008-9393-5](https://doi.org/10.1007/s11214-008-9393-5)
- S.P. Slinker, J.A. Fedder, J.G. Lyon, Plasmoid formation and evolution in a numerical simulation of a substorm. *Geophys. Res. Lett.* **22**, 859 (1995)

- B.U.O. Sonnerup, L.J. Cahill, Magnetopause structure and attitude from Explorer 12 observations. *J. Geophys. Res.* **72**, 171 (1967)
- B.U.O. Sonnerup, L.J. Cahill, Explorer 12 observations of the magnetopause current layer. *J. Geophys. Res.* **73**, 1757 (1968)
- R.J. Strangeway, J. Raeder, On the transition from collisionless to collisional magnetohydrodynamics. *J. Geophys. Res.* **106**, 1955 (2001)
- G. Toth, The $\nabla \cdot B$ constraint in shock-capturing magnetohydrodynamics codes. *J. Comput. Phys.* **161**, 605 (2000)
- E.R. Tufte, *Envisioning Information* (Graphics Press, Cheshire, 1990)
- V.M. Vasyliunas, Mathematical models of magnetospheric convection and its coupling to the ionosphere, in *Particles and Fields in the Magnetosphere* (Dordrecht, Reidel, 1970), p. 61
- M. Wiltberger, T.I. Pulkkinen, J.G. Lyon, C.C. Goodrich, MHD simulation of the magnetotail during the December 10, 1996, substorm. *J. Geophys. Res.* **105**, 27,649 (2000)
- S.T. Zalesak, Fully multidimensional flux-corrected transport. *J. Comput. Phys.* **31**, 355 (1979)
- S.T. Zalesak, Very high order pseudospectral flux-corrected transport (FCT) algorithms for conservation laws, in *Proceedings of the Fourth IMACS International Symposium on Computer Methods for Partial Differential Equations*, ed. by R. Vichnevetsky, R.S. Stepleman (IMACS, Rutgers University, New Brunswick, 1981), p. 126